Size-distribution evolution of ion-beam-synthesized nanoclusters in silica

C. W. Yuan,[1,2] D. O. Yi,[1,2] I. D. Sharp,[3] S. J. Shin,[1,2] C. Y. Liao,[1,2] J. Guzman,[1,2] J. W. Ager III,[2] E. E. Haller,[1,2] and D. C. Chrzan[1,2]

[1]*Department of Materials Science and Engineering, University of California, Berkeley, California 94720, USA*
[2]*Materials Sciences Division, Lawrence Berkeley National Laboratory, Berkeley, California 94720-1760, USA*
[3]*Walter Schottky Institut, Technische Universität München, Am Coulombwall 3, 85748 Garching, Germany*

(Received 11 June 2009; revised manuscript received 21 September 2009; published 22 October 2009)

A model to describe the growth of nanoclusters in silica via ion-beam synthesis is introduced. Kinetic Monte Carlo simulations indicate that nucleation, growth, coarsening, and fragmentation occur throughout implantation, leading to a steady-state size-distribution shape that agrees with experimental observations. A set of coupled rate equations are derived and solved within a self-consistent mean-field approximation. An intermediate asymptotic scaling analysis helps to identify the important experimentally accessible parameters that control ion-beam-synthesized nanocluster size distributions. The model predicts that the shape of the as-implanted size distribution depends only on a characteristic length governed by the effective diffusivity, effective ion solubility, and the volumetric flux while the average cluster size is determined by the solute/matrix interface energy.

DOI: 10.1103/PhysRevB.80.134121 PACS number(s): 81.07.−b, 61.72.U−, 61.80.−x, 81.15.Jj

I. INTRODUCTION

Far-from-equilibrium solid-state dynamics driven by ion irradiation/implantation has had a long history in modern science and remains a frontier of research for nuclear materials development and electronic device processing.[1–6] An example of this far-from-equilibrium growth process is found in the ion-beam synthesis (IBS) of nanocrystals. In IBS, energetic ions are implanted into a suitable matrix in which their solubility is low.[7,8] The embedded ions are mobile within the matrix and can encounter other atoms even during implantation. These encounters lead to cluster nucleation and growth. However, cluster growth is necessarily accompanied by ion-induced collision cascades. The damage causes the clusters to break into fragments and limits their maximum size.[9] This basic understanding of IBS has been exploited to fabricate interesting nanostructures[9–15] and alter cluster size distributions.[6,8,9,15]

However, unlike low-dose semiconductor doping via implantation, that employs doses approximately four orders of magnitude lower than those employed in IBS, and is extensively studied and understood,[16–19] no detailed, comprehensive, quantitative theory has been developed for predicting and controlling the nanocrystal size distribution produced by IBS. Moreover, the minimal set of parameters required to predict the shape of the cluster size distributions arising from IBS has not been determined.

An effort to describe a quantitatively size distribution during IBS was described.[20] This study assumed that nucleation and growth were delayed until after implantation. The model included the nucleation, growth, and coarsening of nanoclusters embedded in a matrix. Quantitative agreement between the self-consistent solution to a set of coupled rate equations and kinetic Monte Carlo (KMC) simulations was obtained. In addition, the solutions were shown to reduce to well-known scaling solutions for coarsening size distributions. However, the model fails to explain the experimentally observed size distributions.[9,21] As a result, an improved model for IBS has been introduced that is built upon the prior work.[22] In this paper, this model and its predictions are described in detail. The model includes the six atomic-scale processes during implantation which are important to growth: (1) ion implantation into an amorphous matrix, (2) the (off-lattice) random walk of implanted atoms, (3) the attachment of atoms to each other and existing clusters, (4) the relaxation of the shape of the clusters, (5) thermally driven cluster dissolution, and (6) impingement-induced fragmentation of clusters. These processes are explored using two different approaches: (1) KMC simulations and (2) the mean-field self-consistent solution to a set of coupled rate equations. The model's predictions for cluster size distributions are presented. The present study focuses solely on the evolution of the cluster size distribution *during* implantation. The model predicts that there are two key parameters governing the as-implanted size distribution for a given material: (1) the characteristic length, $L \equiv (Dn_\infty/F)^{1/2}$, where F is the volumetric implantation rate, n_∞ is the effective solute solubility, and D is the (effective) diffusivity of the implanted ions, and (2) the interface energy between the matrix and growing clusters, γ.

II. KINETIC MONTE CARLO MODEL OF ION MIXING, NUCLEATION, AND GROWTH

In a kinetic Monte Carlo simulation, one identifies the key kinetic processes of the system and assigns rates of occurrence to these processes. In our model of IBS, the six aforementioned kinetic processes are included in the KMC simulation as described below.

The introduction of ions into the matrix is governed by the implantation rate F, defined as the number of atoms implanted per unit volume per unit time. Experimental values of F can be computed by taking the reported areal dose rate and considering the depth of the implantation profile. The actual rate of the implantation event is computed by multiplying the volumetric implantation rate by the system cell

size, and the act of implantation is carried out by making an atom of the implanted species appear in a randomly chosen location within the simulation cell.

Once atoms are inside the system, they may roam throughout three-dimensional space. Within KMC, the atoms go through thermally activated hopping events from metastable site to metastable site within the amorphous matrix. These off-lattice monomer hopping events occur in random directions and drive the relaxation of the far-from-equilibrium system. In the context of implantation, atomic mobility can be enhanced by the excess concentration of point defects resulting from the collision cascade, as in the phenomenon of transient-enhanced diffusion.[18,23] If one may characterize this Brownian atomic motion by its equilibrium parallel, D, then the random hopping events occur at a relaxation rate $r_{migration}=\frac{6D}{a^2}$, where D is the (transient-enhanced) diffusivity of the implanted atom in the matrix. The hop distance, a, is taken to be $a=5$ Å, roughly the cube root of the volume of a SiO_2 formula unit in the oxide.[24]

When a monomer meets another monomer or cluster during its movement, attachment takes place instantly whenever the distance between the particles is within a capture length r_{cap}, measured between the surfaces of the reacting species. Hence, there is no adsorbing state within the model. For this work, we set $r_{cap}=0$.

Cluster relaxation is driven by a reduction in surface energy. Under most circumstances, the interface energy is anisotropic and the resulting Wulff shapes can be quite complex. For simplicity, we assume that interface energies are isotropic, and that relaxation of the clusters to equilibrium spherical shapes is rapid compared to the time scales associated with other kinetic processes in the problem. Consequently, whenever an adatom contacts a cluster or another atom, the cluster is assumed to become spherical immediately, with volume equal to the sum of its constituent atoms. The volume of each Ge atom is taken to be 22.7 $Å^3$, the volume per atom in the crystalline phase. Changing the isotropic interface energy assumption will alter details of the predictions but the gross features of the size distributions are not expected to change. The relaxation process conserves the center of mass of the adatom and cluster, and thereby imparts a small mobility to clusters.

Atom dissolution occurs when one of the constituent atoms becomes detached from the host cluster. All atoms on the surface of a cluster are assumed to have equal probability of detachment and once an atom detaches, it moves to a random location on the surface, with its surface a detachment distance r_{cap} away (measured normal to the cluster surface). In the present study, $r_{cap}=0$.

The detachment event creates a monomer within the matrix and also shifts the position of the original host particle to conserve center of mass. Hence, after each detachment event, distances between the atom and all other particles are checked for instant relaxation, with the only exclusion being the distance between the formed atom and its original host. The same exclusion applies when distance checking for the shifted original host particle. However, it is possible that a series of cascading relaxational events occur that lead to local clustering of mass that includes both the detached atom and its original. Therefore, the exclusion in instant relaxation only applies between the detached atom and its original host particle (for the current iteration). If either one becomes absorbed to form a species, then the restriction on the distance-checking routine is lifted.

For a cluster of size R, the rate of desorption is[20,25]

$$r_{detachment}=4\pi R^2\frac{D}{a}n_\infty \exp\left(\frac{2\gamma\Omega}{Rk_BT}\right), \tag{1}$$

where $\frac{6D}{a}=\frac{6D}{a^2}a$ is the "velocity" of diffusing atoms and $\frac{1}{6}n_\infty \exp(\frac{2\gamma\Omega}{Rk_BT})$ is the local concentration of atoms that diffuse radially outward from the spherical cluster. Here γ is the interfacial energy between the precipitate and the matrix and Ω is atomic volume of the implanted species. [Detailed derivation of Eq. (1) can be found in the work of Yi *et al.*[20]] It should be noted that the Gibbs-Thomson relation, $n(r)=n_\infty \exp(\frac{2\gamma\Omega}{Rk_BT})$, employed above to describe the equilibrium concentration of solute atoms at the matrix-cluster interface, contains information about the critical nucleus size defined in homogeneous nucleation theory, $r_{critical}=\frac{-2\gamma}{\Delta G_v}$, where ΔG_v is the free-energy change per volume of precipitation. $n_\infty=n_s \exp(\frac{-E_f}{k_BT})$ is solubility of the solute species in the matrix at the given temperature, where n_s is the density of sites and E_f is the internal energy change upon removing a solute atom from its bulk phase (reference state) and placing it inside the matrix. This formation energy, together with the contribution from configurational entropy, approximates the chemical potential of the solute atom inside the matrix. In the limit of very low solubility, and noting that the reference state is taken to be the bulk phase of the implanted species, one may define

$$r_{critical}=\frac{-2\gamma}{\Delta G_v}=\frac{-2\gamma\Omega}{\mu_{bulk}-\mu_{solution}}=\frac{2\gamma\Omega}{E_f+k_BT\ln c}, \tag{2}$$

where c is the number-per-site of the solute atoms. Equation (2) allows one to relate the relaxation model to fundamental theories of phase transformation.

For computational efficiency, the effect of ion impingement on a cluster is modeled with a coarse-grained approach. Following Heinig and co-workers,[9] we employ a scheme wherein each collision cascade displaces every atom in an impacted cluster in a random direction by a distance r governed by a Poisson displacement probability distribution,

$$p(r)=\frac{1}{8\pi\lambda^3}\exp(-r/\lambda). \tag{3}$$

The characteristic length λ reflects the ion mass and energy, and is determined by fitting the displacement profiles for an ion-damaged embedded slab computed using TRIM,[26] as is done by Heinig *et al.*[9] Typical values of λ range between 3 and 5 Å. (A more detailed description of the process is presented below.)

After all atoms within a cluster are scattered from an ion blast, the system is once again allowed to relax instantly, as atoms and clusters that "touch" each other are bonded together. When a cluster is fragmented and relaxed according to this scheme, the result is a power-law fragment size distribution. Such power-law fragment size distributions have

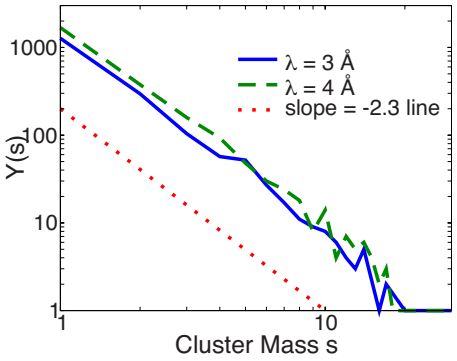

FIG. 1. (Color online) Fragment size distribution after an impingement followed by relaxation, as compared with KMC results. $Y(n)$ is the number of clusters consist of n atoms. A slope of −2.3 is reported by Kissel and Urbassek (Ref. 27) for sputtering of a spherical Au cluster modeled with molecular dynamics.

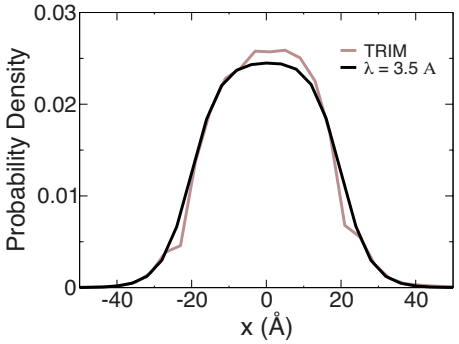

FIG. 3. (Color online) Normalized Ge recoil distribution as a result of implanting 120 keV Ge ions into a 4 nm Ge slab embedded within SiO_2 100 nm below the surface as computed by TRIM. The 4 nm slab is centered at zero. The predictions stemming from Eq. (3) with λ=3.5 Å are also shown.

been observed in both molecular-dynamics simulations[27] and sputtering experiments.[28] This coarse-grained description of the cascade provides a good description of the results of a cascade. Specifically, molecular-dynamics simulations of Au ions impacting free-standing Au clusters yield a fragment size distribution that is characterized by a power-law distribution of small fragments, $f_s \sim s^{-\alpha}$, with f_s the number of fragments with s atoms, and $\alpha=2.3$.[27] Modeling the same process using KMC as described here yields the same exponent. Further, the exponent appears to be independent of ion mass and energy, as shown in Fig. 1.

An example of the effect of ion impingement is illustrated in Fig. 2, where an initial spherical Ge cluster of radius 2 nm undergoes an end-of-range damage cascade caused by a Ge ion that started with 120 keV outside of the matrix. The result is a smaller central cluster surrounded by collection of nearby smaller fragments, with a size distribution as described in Fig. 1. For this simulation λ=3.5 Å, a value obtained by first performing a TRIM (Ref. 26) implantation simulation for the case of a 4 nm Ge slab embedded within SiO_2 at the average implant depth for 120 keV Ge ions. The resultant Ge recoil distribution, which may be converted to the displacement probability distribution of atoms dislodged from within the slab, is then fit to the normalized form of the atomic displacement distribution described before, with λ as the only fitting parameter, as shown in Fig. 3. Note that TRIM indicates that an average of 5.9 keV is transferred to the recoils from the 4 nm slab per ion collision. Since the estimated total interface energy difference (using the present theory to estimate the interface energy) between the "before" and "after" configurations in Fig. 2 is roughly 3.2 keV, the calculation suggests that there is ample energy available during the collision cascade for creating the observed clusters.

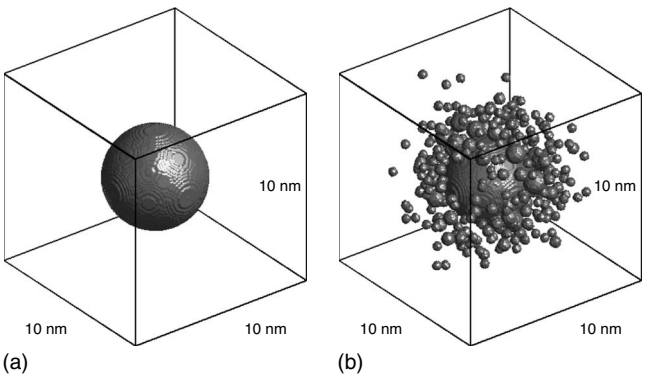

FIG. 2. (a) A 2 nm radius cluster. Box dimension $L=10$ nm. (b) After undergoing an end-of-range damage cascade induced by an ion with prematrix energy of 120 keV, the system becomes a smaller cluster surrounded by a power-law distribution of fragments, as depicted in Fig. 1

Unless otherwise noted, the KMC results presented below are obtained by imposing periodic boundary conditions upon a cubic cell with and edge length of 30 nm. (Note that atom hopping, which takes place at Angstrom scales, is still off-lattice.) Statistics are obtained by averaging over 30 simulations. Cluster size distributions are obtained by binning clusters according to radii, using bin widths of 1 Å. Statistical errors are computed as the standard deviation of the 30 simulations divided by the square root of the number of independent trials (typically 30). The error bars so computed are not resolvable on the scale of the plots, and for clarity, have been omitted.

III. RATE EQUATIONS

A mean-field approach to model nanocluster size-distribution evolution in during IBS is also employed not only to complement KMC but also to provide analytical insight into the behavior of the system. Based on relaxational theories in the literature,[20,29,30] a set of coupled rate equations (RE) are derived with terms added to describe the effects of cluster fragmentation. Assuming that an ion-cluster collision event breaks the cluster into a power-law distribution of fragments, one constructs the following set of coupled differential equations:

$$\frac{d\langle n_1\rangle}{dt} = F - 2D\sigma_1\langle n_1\rangle^2 - D\sum_{j>1}\sigma_j\langle n_j\rangle\langle n_1\rangle + 2\frac{\langle n_2\rangle}{\tau_2} + \sum_{j>2}\frac{\langle n_j\rangle}{\tau_j} + F\Omega\sum_{j>1}\langle n_j\rangle(j+1)K_1(\alpha,j), \quad (4)$$

$$\frac{d\langle n_s\rangle}{dt} = D\sigma_{s-1}\langle n_{s-1}\rangle\langle n_1\rangle - D\sigma_s\langle n_s\rangle\langle n_1\rangle - \frac{\langle n_s\rangle}{\tau_s} + \frac{\langle n_{s+1}\rangle}{\tau_{s+1}} - F\langle n_s\rangle\Omega(s+1) + F\Omega\sum_{j>s}\langle n_j\rangle(j+1)K_s(\alpha,j), \quad (5)$$

where $\langle n_s\rangle$ is the average density of clusters containing s atoms, D is the effective diffusivity within the matrix that characterizes the rate of relaxation, σ_s is the capture length for a cluster of size s to capture a diffusing monomer, and τ_s is the typical amount of time between individual desorption events from an s cluster. The values of σ_s and τ_s are solved for self-consistently as done by Yi *et al.*[20] The terms of Eqs. (4) and (5) that depend on the volumetric flux rate F are the driven/fragmention parts of the implantation process. Here Ω is the atomic volume and the term $\langle n_j\rangle\Omega(j+1)$ gives the probability of collision between an implanted monomer and a j cluster. $K_s(\alpha,j)$ is a kernel indicating the number of s clusters generated as a result of a fragmented j cluster, where the parameter α characterizes the slope of the power-law fragment distribution arising from an N cluster and appears to be independent of ion mass and energy (α=2.3),

$$K_s(\alpha,j) = A(j,\alpha)s^{-\alpha} \quad (6)$$

with the normalization condition

$$j = \sum_{s=1}^{j-1} A(j,\alpha)s^{-\alpha}s = A(j,\alpha)\sum_{s=1}^{j-1} s^{1-\alpha}. \quad (7)$$

The form of Eq. (6) is motivated by the results of molecular-dynamics simulations[27] and our KMC formulation (see Fig. 1). It will be shown below that a typical implantation arrives at a steady-state profile as a result of the balance between the fragmentation and relaxation mechanisms.[9] Mathematically, it is simple to find this steady-state solution. The derivation begins with the identity

$$P(s) = \frac{s\langle n_s\rangle}{\sum_{s=1}^{\infty} s\langle n_s\rangle}, \quad (8)$$

which defines the probability of an atom residing in a cluster of size s, $P(s)$. At steady state, $\frac{dP(s)}{dt}=0$. With the knowledge that $\Sigma_{s=1}^{\infty}s\langle n_s\rangle = Ft$ and $\Sigma_{s=1}^{\infty}s\frac{d\langle n_s\rangle}{dt}=F$, one obtains the following expression by differentiating Eq. (8) with respect to time,

$$\frac{d\langle n_s\rangle}{dt} = \frac{\langle n_s\rangle\sum_{s=1}^{\infty} s\frac{d\langle n_s\rangle}{dt}}{\sum_{s=1}^{\infty} s\langle n_s\rangle} = \frac{\langle n_s\rangle}{t}. \quad (9)$$

Equation (9) allows for direct computation of the steady-state size distribution during implantation. By substituting Eq. (9) into Eqs. (4) and (5), it is possible to solve numerically for the steady state $\langle n_s\rangle$ for a given set of D, F, n_∞, and γ, in the limit of large t.

This set of steady-state rate equations can be put into dimensionless form by scaling all lengths by $L=(Dn_\infty/F)^{1/2}$ and all times by n_∞/F, yielding

$$\frac{\langle\tilde{n}_1\rangle}{\tilde{t}} = \tilde{n}_\infty - 2\tilde{\sigma}_1\langle\tilde{n}_1\rangle^2 - \sum_{j>1}\tilde{\sigma}_j\langle\tilde{n}_j\rangle\langle\tilde{n}_1\rangle + 2\frac{\langle\tilde{n}_2\rangle}{\tilde{\tau}_2} + \sum_{j>2}\frac{\langle\tilde{n}_j\rangle}{\tilde{\tau}_j} + \tilde{n}_\infty\tilde{\Omega}\sum_{j>1}\langle\tilde{n}_j\rangle(j+1)K_1(\alpha,j) \quad (10)$$

and

$$\frac{\langle\tilde{n}_s\rangle}{\tilde{t}} = \tilde{\sigma}_{s-1}\langle\tilde{n}_{s-1}\rangle\langle\tilde{n}_1\rangle - \tilde{\sigma}_s\langle\tilde{n}_s\rangle\langle\tilde{n}_1\rangle - \frac{\langle\tilde{n}_s\rangle}{\tilde{\tau}_s} + \frac{\langle\tilde{n}_{s+1}\rangle}{\tilde{\tau}_{s+1}} - \tilde{n}_\infty\tilde{\Omega}\langle\tilde{n}_s\rangle\times(s+1) + \tilde{n}_\infty\tilde{\Omega}\sum_{j>s}\langle\tilde{n}_j\rangle(j+1)K_s(\alpha,j). \quad (11)$$

The tildes represent dimensionless versions of dimensioned quantities. It is noted that $\tilde{n}_\infty=\tilde{F}$ and that $\tilde{D}=1$.

Typically, one is interested in studying the size distribution in radius space to make connection to experimentally observed data. To that end, only cluster sizes of $s\gg 1$ are of practical concern due to the $s^{1/3}$ dependence of a cluster radius. Therefore, one may simplify the analysis further by expanding $1/\tau_s$ in Eq. (11) in terms of other parameters,[20] under the assumption that $R_s\approx R_{s-1}+r_{cap}$,

$$\frac{\langle\tilde{n}_s\rangle}{\tilde{t}} = \tilde{\sigma}_{s-1}\langle\tilde{n}_{s-1}\rangle\langle\tilde{n}_1\rangle - \tilde{\sigma}_s\langle\tilde{n}_s\rangle\langle\tilde{n}_1\rangle - \langle\tilde{n}_s\rangle\tilde{\sigma}_{s-1}\tilde{n}_\infty\exp(\tilde{\Gamma}/\tilde{R}_s) + \langle\tilde{n}_{s+1}\rangle\tilde{\sigma}_s\tilde{n}_\infty\exp(\tilde{\Gamma}/\tilde{R}_{s+1}) - \tilde{n}_\infty\tilde{\Omega}\langle\tilde{n}_s\rangle(s+1) + \tilde{n}_\infty\tilde{\Omega}\sum_{j>s}\langle\tilde{n}_j\rangle(j+1)K_s(\alpha,j), \quad (12)$$

where $\Gamma=\frac{2\gamma\Omega}{k_BT}$, the capillary length. Since the capture length, σ_s, is solved for self-consistently from the solution $\langle n_s\rangle$, and α is treated as a constant, the steady-state solution of Eq. (12) formally depends only on $\tilde{t}$, $\tilde{n}_\infty$, $\tilde{\Omega}$, and $\tilde{\Gamma}$. These four parameters and specific influence on the steady-state solution are discussed below.

IV. RESULTS AND DISCUSSION

For an initial calculation, we consider parameters near those appropriate for the implantation of Ge into amorphous silica carried out by Sharp and co-workers.[21] The total ion dose reflects the experimental final density at around 6 at. % ($N_0=4\times10^{21}$ cm^{-3}) and the parameter λ is taken to be 3.5 Å, corresponding to the end-of-range impact strength of Ge implanted with 120 keV initial energy (as indicated by TRIM). The implantation rate is set to be $F=F_0=10^{-6}$ A^{-3} s^{-1}, roughly a factor of seven higher than a typical experimental value, $F_{exp}=1.5\times10^{-7}$ A^{-3} s^{-1} (corresponding to 1.5×10^{12} cm^{-2} s^{-1} when taking into account the 100 nm of implant depth), to enable reasonable computation times. The effective diffusivity (D) during ion irradiation is unknown and is set here to be $D=D_0=6.47\times10^{-10}$ cm^2 s^{-1}, where D_0 is the approximated room-temperature diffusivity of Ge in silica.[24] The effective solubility of Ge in SiO_2 during implantation at room temperature is taken to be $n_\infty=1.01\times10^8$ cm^{-3}. Below, we deduce that the Ge/SiO_2 interface energy is near 1.5 J m^{-2}.

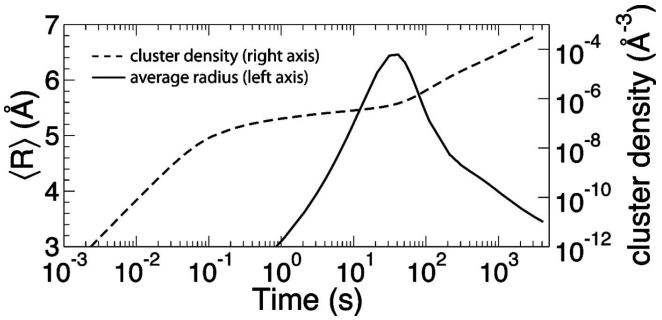

FIG. 4. The average cluster radius (solid line, left axis) and the cluster number density (dashed line, right axis) as a function of time for typical growth conditions, based on rate-equations calculations.

However, choosing interface energies this large increases the critical cluster size for nucleation, and the associated simulations require substantial computational resources. Thus the Ge/silica interface energy is set to 0.2 J m^{-2} for these initial calculations.

Typical results are shown in Fig. 4 (RE) and Fig. 5 (KMC). Figure 4 plots both the average radius of the clusters, $\langle R \rangle$,

$$\langle R \rangle = \frac{1}{N} \sum_{i=1}^{N} R_i \tag{13}$$

with the index i running over all clusters, R_i the radius of cluster i, and N the total number of clusters, as well as the cluster number density as a function of time. In the earliest stage (before 0.1 s), the number of clusters increases rapidly as a result of many nucleation events. Between 0.1 and 30 s, coarsening of the clusters commences, hence the number density of clusters rises slowly while the average radius of the clusters rises rapidly. Up to this point, the effect of fragmentation has been negligible relative to other processes due to the low concentration and small size of the clusters, and the growth process is similar to that observed in two-dimensional (2D) nucleation and growth models, as shown in Fig. 5(a). The effect of fragmentation gradually becomes significant as both the concentration and the size of the clusters rise, raising the likelihood of ion damage. This eventually leads to a peak in $\langle R \rangle$ and the average cluster size starts to decrease. As more mass becomes implanted into the matrix, ion damage helps to redistribute mass and create more fragments. For times larger than 30 s, the clusters continue to be damaged, the average radius decreases, and the volume fills rapidly with clusters [Figs. 5(b) and 5(c)]. In the final stages of growth $\langle R \rangle$ approaches a steady-state value.

Figure 6 compares KMC and RE results for the evolution of a cluster size distribution during implantation, using the aforementioned parameters. The two computational approaches display good agreement during the various stages the system undergoes during implantation. In Fig. 6(a), at less than 1% of the total dose, the effect of damage cascade is negligible and the distribution evolves as a purely nucleation-and-growth system with external input of mass. However, as more atoms are introduced into the matrix and the clusters become larger, as shown in Fig. 6(b), the amount

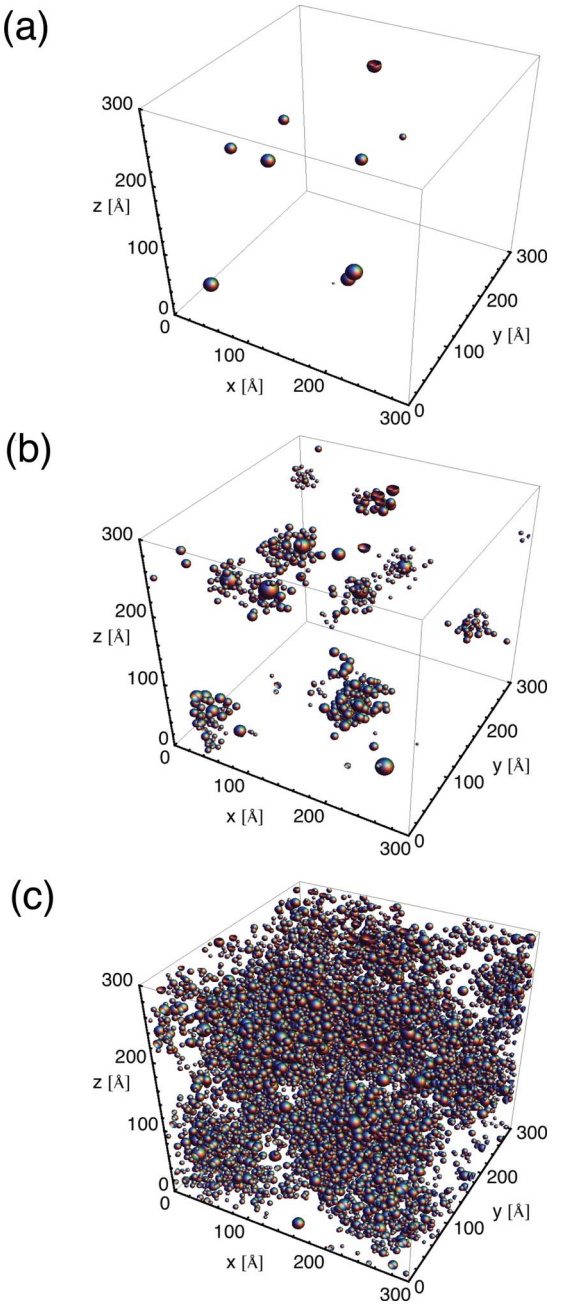

FIG. 5. (Color online) Microstructural evolution (a) at 30 s, (b) at 300 s, and (c) at 3000 s from KMC simulations (see text).

of mass transferred from the larger sizes to the smaller sizes becomes appreciable, and a bimodal size distribution appears. As implantation continues, clusters grow while some of them experience fragmentation and the bimodal distribution becomes wider and more weighted toward the smaller particles, as displayed in Fig. 6(c). The second peak at large sizes eventually disappears, leading to a unimodal profile of smaller particles. Finally, by the end of implantation, the system gravitates toward a log-normal-like distribution, as shown in Fig. 6(f).

Another comparison between KMC and RE results, this time with the interface energy equal to 0.5 J m^{-2}, is shown in Fig. 7. Again, the two approaches display near-

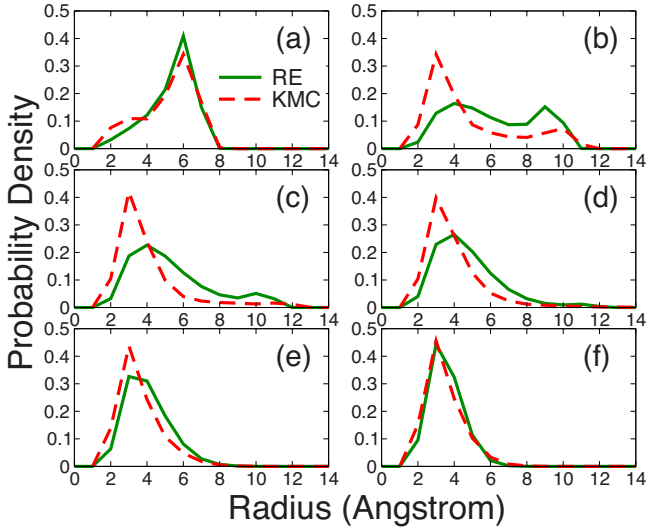

FIG. 6. (Color online) (a) KMC (dashed line) and RE (solid line) size distributions at 0.27% of the experimental final density, with $\lambda=3.5$ Å, $\alpha=2.3$, $F=F_0=10^{13}$ cm^{-2} s^{-1}, $D=D_0=6.47\times10^{-10}$ cm^2 s^{-1}, $n_\infty=1.01\times10^8$ cm^{-3} and the interface energy $\sigma=0.2$ J m^{-2}. (b) 1.49%. (c) 2.70%. (d) 5.14%. (e) 27.0%. (f) As implanted. The bin size is 1 Å. Error bars for the KMC results are small enough to be omitted for clarity of display.

quantitative agreement throughout the evolution of the size distribution. It should be noted that increasing the value of the interface energy effectively increases the size of the critical nucleus in nucleation and growth. This implies that, instead of forming many small clusters during the nucleation stage, the system prefers forming fewer, larger clusters. Not only are these large supercritical nuclei stronger sinks for monomer attachment than smaller ones, they also coarsen more quickly due to the exponential dependence of desorption rate on Γ in Eq. (1),[20] hence they grow faster and extend the overall width of the size distribution. This impact is manifested when one compares Fig. 6 to Fig. 7. In Fig. 6, the interface energy employed is 0.2 J m^{-2}, which translates to roughly a critical nucleus radius of 1 Å, according to Eq. (2). This value is obtained if one takes E_f to be 0.88 eV (from Carbonaro *et al.*[31]), $\Omega=22.7$ Å^3 (from the molar volume of Ge at room temperature) and $c\approx6\times10^{-6}$ (empirically taken from RE simulations by noting the mass density at which stable clusters of size $s\geq2$ begin to form), and this value of $r_{critical}$ is smaller than the radius of a single Ge atom, 1.76 Å. Therefore, every species in Fig. 6 is supercritical and one observes no peak arising from the population of subcritical particles. On the other hand, for $\gamma=0.5$ J m^{-2}, the critical nucleus size becomes 2.47 Å, calculated using the same parameters described above. A supercritical nucleus therefore must consist of at least three Ge atoms. The result is the observation of a large population of monomers and two-atom clusters at the very early stages of implantation, when the effect of fragmentation is negligible and nucleation and growth is the dominant mechanism of cluster formation. This peak at the one-atom and two-atom range arises due to the frequent attachment/detachment reactions of these two species, which are the most numerous. Monomers frequently run into each other to form two-atom clusters, only to break apart into monomers again due to instability. Beyond the two-atom clusters, a structure appears that resembles a driven, coarsened distribution. This is illustrated in Fig. 7(a). Later on, as collision cascades become more frequent, the majority of the clusters in the system come from scattered fragments and the bimodal structure disappears.

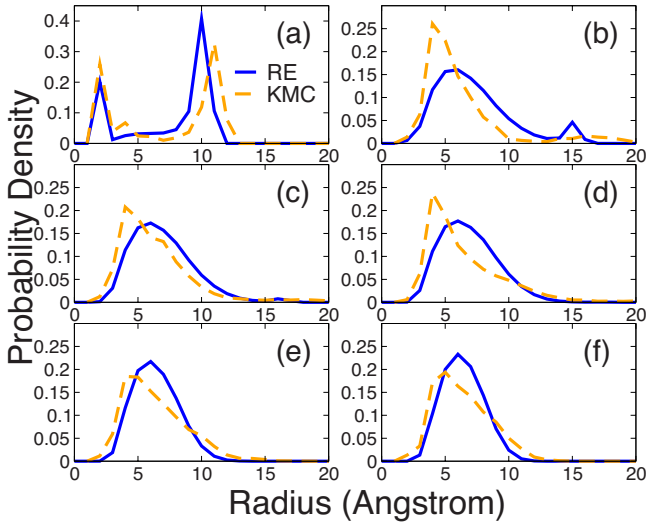

FIG. 7. (Color online) (a) KMC (dashed line) and RE (solid line) size distributions at 0.27% of the experimental final density, with $\lambda=3.5$ Å, $\alpha=2.3$, $F=F_0=10^{13}$ cm^{-2} s^{-1}, $D=D_0=6.47\times10^{-10}$ cm^2 s^{-1}, $n_\infty=1.01\times10^8$ cm^{-3} and the interface energy $\sigma=0.5$ J m^{-2}. (b) 1.49%. (c) 2.70%. (d) 5.14%. (e) 27.0%. (f) As implanted. The bin size is 1 Å.

The agreement between the KMC simulations and RE theory warrants further discussion. The kinetic Monte Carlo scheme simulates a series of stochastic processes that are inherently local, in contrast to the rate theory that assumes all interactions are characterized by mean-field quantities averaged over all of space. While agreement between the two approaches for the purely relaxational case is analyzed and documented,[20] its is still somewhat surprising to observe their concurrence *throughout* the implantation process in the IBS model. This is because the fragmentation event introduces into the stochastic model a length scale, λ, that governs the mass displacement distance upon collision, with the result being a smaller central cluster surrounded by hovering fragments, as shown in Fig. 2. This length scale is not accounted for in the mean-field theory, yet the two models display good agreement on their overall behaviors. One explanation is that the fragmentation event has a similar effect as the desorption event by evaporating mass from the original cluster to locations nearby. The mean-field approximation applied to the purely relaxational case therefore carries over to the study of ion-beam synthesis. However, the length scale λ could still play a major role in the difference between the KMC and RE results.

One discrepancy between the KMC and RE models arises from the treatment of the fragment size distribution in the rate equations. The mean-field theory assumes that each impingement breaks up the impacted cluster completely into a continuous distribution of smaller fragments, whose size distribution is characterized by a power-law function. However,

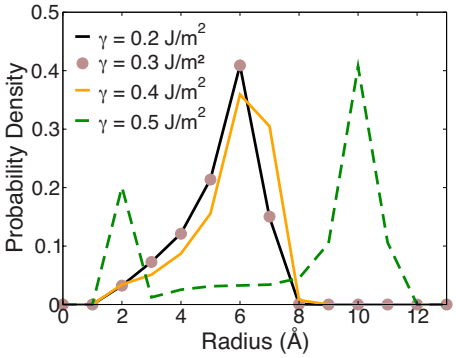

FIG. 8. (Color online) RE size distributions at 0.27% of the experimental final density, with γ=0.2, 0.3, 0.4, and 0.5 J m^{-2} and other parameters identical to those used in Fig. 6. The bin size is 1 Å.

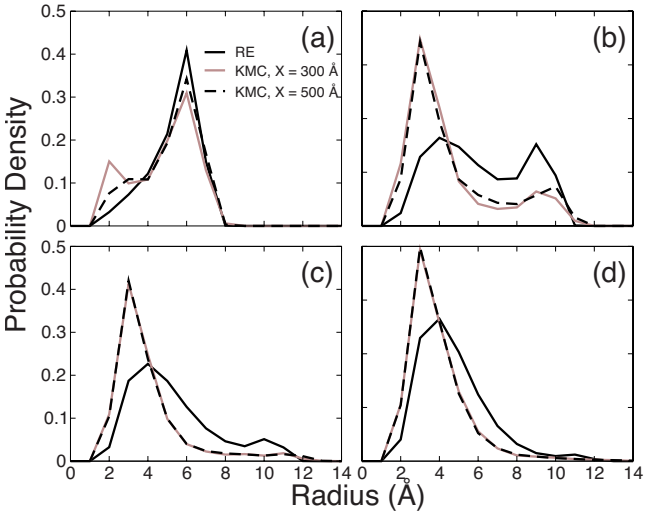

FIG. 9. (Color online) (a) KMC (dashed gray line) size distributions from different simulation box sizes and RE (solid line) size distribution at 0.27% of the experimental final density, with parameters identical to those used in Fig. 6 and X is the length of the cubic KMC cell. (b) 1.49%. (c) 2.70%. (d) 5.14%. The bin size is 1 Å. Error bars for the KMC results are omitted for clarity of display.

that is clearly not what is seen in Figs. 1 and 2, where most of the original cluster remains. The rate theory's treatment of fragmentation events is therefore an overkill of the actual process it aims to describe. The impact of this overestimation is negligible when the cluster sizes are not large in comparison to λ, meaning the KMC collision event would result in sufficient local mixing such that the mean-field theory's approximation on the fragment size distribution is acceptable. On the other hand, one may imagine the disagreement to widen as the clusters involved become larger. This overestimation of the cluster breakup process possibly contributes to the lesser agreement between the KMC and RE results in Fig. 7(f) in comparison to Fig. 6(f).

The effect of the critical nucleus size is further illustrated in Fig. 8, where early-stage size distributions from rate-equation calculations using different values of γ are compared. It should be noted that, for γ=0.2, 0.3, 0.4, and 0.5 J m^{-2}, the critical nucleus radius is 0.99, 1.48, 1.98, and 2.47 Å. That means, for both γ=0.2 and 0.3 J m^{-2}, the single Ge atom is already a stable, supercritical particle. Consequently, their early-stage distributions look practically identical. On the other hand, when γ=0.4 J m^{-2}, the critical size surpasses the radius of a monomer, and the number of atoms in a stable particle changes from one single atom to two atoms (r=2.21 Å). This discrete jump results in a larger average size but does not yet produce a bimodal structure because every single monomer, upon attachment, becomes stable. If the critical nucleus size is larger than two atoms, then monomers will frequently run into each other and breakup soon after, resulting in a peak at the one-atom and two-atom range, opposite of the coarsening peak.

The impact of finite size on simulation results is analyzed in Fig. 9. At the very early stage, when the overall number of atoms in the KMC simulation cell is low and the average distance between critical clusters is large, the agreement between the KMC and rate equations is seen to improve upon increasing the cell size. However, this improvement is no longer discernible beyond ≈2.7% of the Ge experimental dose, which is about 1×10^{15} cm^{-2}. This implies that finite-size effects in the KMC simulations are negligible at practical solute concentrations. This observation, along with the good agreement between KMC and rate equations results at higher doses (as shown in Figs. 6 and 7) suggests that finite-size effects are negligible at sufficiently high doses, and that the self-consistent mean-field approach for analyzing size-distribution evolution in ion-beam synthesis is valid.

It is observed empirically that the cluster size distribution reaches a steady state. As this limit is approached, the shape of the cluster size distribution changes slowly and the steady-state shape serves as a good description of the shape of the cluster size distribution during the latter stages of implantation. In this high-dose regime, the agreement between the rate equations and KMC results indicates that one can employ the rate-equation-based description for quantitative analysis of the asymptotic behavior. The analysis likely applies to most real experimental systems since the profile evolves very slowly toward the asymptotic solution, as evidenced by Fig. 6 and 7.

Solving Eqs. (10) and (11) for large times yields the steady-state cluster size distribution. As concluded following the analysis of Eq. (12), the steady-state size distribution formally depends on four parameters: $\tilde{t}$, $\tilde{n}_\infty$, $\tilde{\Omega}$, and $\tilde{\Gamma}$. However, if one evaluates $\tilde{t}$ and $\tilde{n}_\infty$ using experimentally believable values, one finds that $\tilde{t}\approx10^{14}$ and that $\tilde{n}_\infty\approx10^{-15}$. On the other hand, $\tilde{\Omega}$ and $\tilde{\Gamma}$ are on the orders of 1–100. This, by the conjecture of intermediate asymptotic analysis,[32] suggests that the steady-state behavior has negligible dependence on $\tilde{t}$ and $\tilde{n}_\infty$. The asymptotic solution therefore should depend on two parameters only: the dimensionless atomic volume, $\tilde{\Omega}=\Omega/L^3$, and $\tilde{\Gamma}$, which is the interface energy, γ, and the temperature. This conjecture is affirmed by numerical solutions; moreover, it is found that the steady-state shape of the distribution depends on $\tilde{\Omega}$, and that γ only impacts the average size (for a given L). This behavior is in marked contrast to the behavior observed during 2D epitaxial

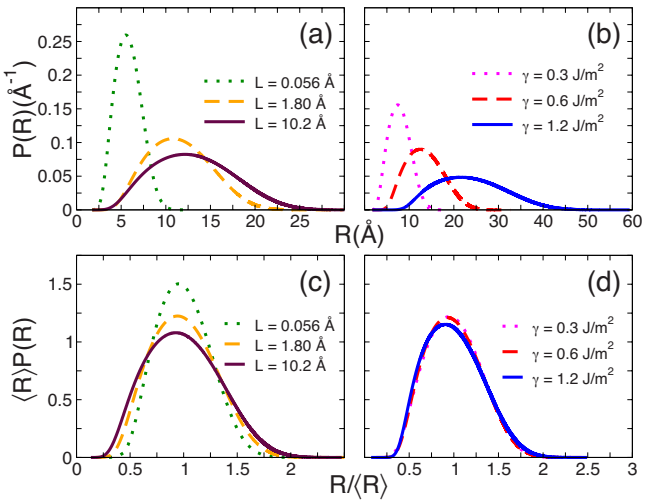

FIG. 10. (Color online) (a) Steady-state size distributions, with γ=0.4 J m^{-2}. (b) Steady-state size distributions, with L=1.8 Å. (c) Size distributions from panel (a) scaled by the average radius, showing the change in width as a function of L. (d) Those from panel (b) scaled by the average radius, showing little shape change as a function of γ.

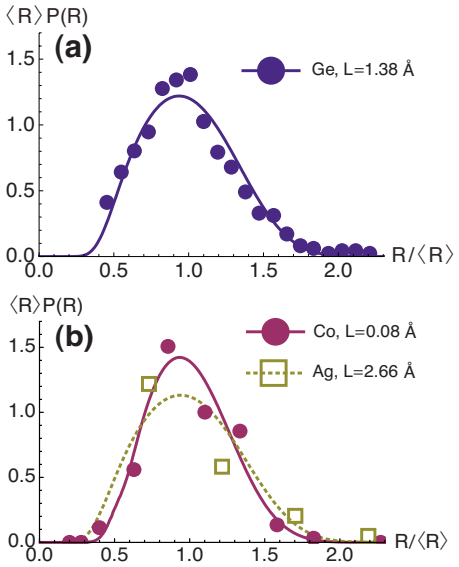

FIG. 11. (Color online) Steady-state shape of the nanocrystal size-distribution function obtained by fitting theory to experimental room temperature as-implanted size distributions for (a) Ge (Ref. 21), (b) Co (Ref. 12), and Ag (Ref. 13). The fits provide an excellent description of the available data.

growth in which the distribution shape is determined by the critical cluster size,[33] a quantity that depends sensitively on γ.

Experimentally speaking, the atomic volume of the implanted species may vary only by a factor of 2 or so from material to material. If this factor of 2 is incorporated into the scaling factor of L^{-3} in the expression of $\tilde{\Omega}$, then the value of L is merely changed by about a factor of 1.3. These changes are small in comparison to the range of $L=(Dn_\infty/F)^{1/2}$, which can change by many orders of magnitude. Therefore, it suffices to say that the length L is the governing parameter for the steady-state shape of the size distribution. Numerically, it is found that increasing L not only increases the average size of the steady-state size distribution but it also widens the relative width of the as-implanted profile, as shown in Figs. 10(a) and 10(c). The experimental value of Dn_∞ likely varies by orders of magnitude between different experimental conditions.[18]

Unlike L, the interfacial tension between the nanoclusters and the host matrix, γ plays a role only in the relaxational part of the model. The value of γ directly impacts the critical nucleus size, which sets the scale of the size of the distribution. In Fig. 10(b), the critical nucleus radius for γ=0.3, 0.6, and 1.2 J m^{-2} would be 1, 5, and 39 atoms (for Ge parameters) and the distributions go through changes in size substantially more than those in Fig. 10(a); however, the shape of the distributions varies negligibly, if it varies at all, as shown in Fig. 10(d). As γ is increased, the number of equations to be solved goes up rapidly due to the exponential increase in critical nucleus size, and numerical noise becomes significant in computing the steady-state solution. This could account for the slight change in shape as observed in Fig. 10(d). Experimentally speaking, the value of γ may be varied by changing the implanted species or the host matrix but it should be noted that experimental values of γ are unlikely to differ by an order of magnitude from those shown in Fig. 10(d). Hence, for all practical purposes, the interface energy does not alter the scaled shape of the as-implanted size distribution but merely sets the absolute size (once the shape has been determined by L).

The aforementioned results suggest that (1) the average size of the as-implanted size distribution may be tuned by changing the implanted species/matrix interface energy and (2) the value of L sets the scaled shape of the as-implanted distribution. Therefore, experimentally measured as-implanted size distributions can be fitted to theory to obtain an estimate for the value of L. Figure 11 displays the fitted curves for three materials. Ge is best fit with a value of L=1.38 Å, Co is described by L=0.08 Å, and Ag is described by L=2.66 Å.[34] For the case of Ge, assuming that coarsening is very slow (as is observed experimentally[10]), we can compare the observed value with the expected value. Using the accepted (normal) diffusion coefficient for Ge in

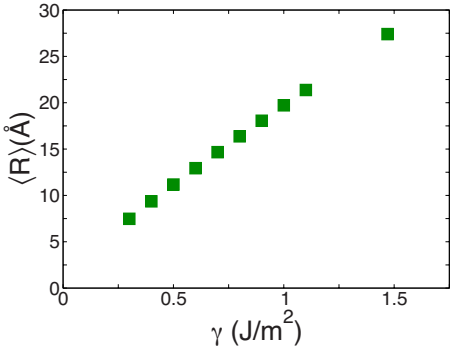

FIG. 12. (Color online) Average radius of the steady-state solution as a function of γ, for L=1.38 Å. A near-linear dependence is observed.

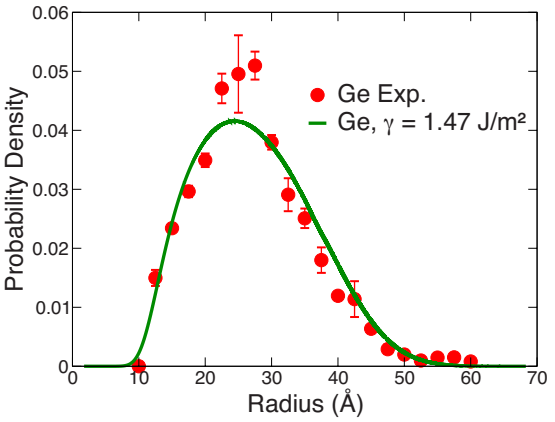

FIG. 13. (Color online) Experimentally measured Ge size distribution (Ref. 21) vs calculated steady-state solution at $L=1.38$ Å and $\gamma=1.47$ J m^{-2}.

silica one predicts $L=0.051$ Å. The measured value for L exceeds the initial prediction by a factor of ≈ 26.4. The implication is that the ratio Dn_∞/F exceeds the expected value by a factor of ≈ 700. This increase, most likely due to ion damage within the matrix, is within the range expected for transient-enhanced diffusion.[18,19] Hence, the values of L needed to model experiments are reasonable. Further, measurements of the shape of the cluster size distribution can be used to obtain information regarding the transient-enhanced diffusion coefficient and the effective diffusivity during implantation.

One may also obtain information regarding the interface energy between the implanted species and the host matrix during implantation from the steady-state behavior. Since the shape of the as-implanted size distribution varies negligibly as a function of γ, once the value of L is determined for a given implantation, the value of γ can be obtained by extrapolating from steady-state solutions of lower values of γ to obtain the experimentally observed average size of the as-implanted clusters. This is shown in Fig. 12, where an approximately linear dependence of the average radius on the interface energy is displayed. Taking $L=1.38$ Å for Ge implanted into amorphous silica, as shown in Fig. 11, one arrives at $\gamma=1.47$ J m^{-2} by extrapolating to the average size (27.1 Å) of the experimentally measured size distribution.[21] The experimental and computed results for the size distribution are shown in Fig. 13. The slight difference in shape between the calculated profile from Fig. 13 and that from Fig. 13(a) is similar to the minute change in shape seen in Fig. 10(d).

The theory also suggests how one might narrow IBS cluster size distributions. Figure 14(a) plots the computed full width at half maximum, scaled by the average cluster radius, $\Delta R/\langle R\rangle$, as a function of L for Ge. Figure 14(b) shows the predicted size distributions. Both sets of data are obtained

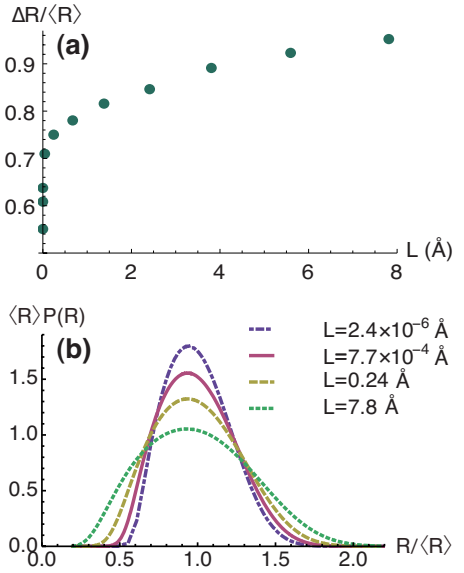

FIG. 14. (Color online) (a) Full width at half maximum plotted as a function of L predicted by the model and (b) the steady-state cluster size distributions expected for different L.

using a fixed interface energy of $\gamma=0.2$ J m^2. As L decreases, so does the width of the cluster size distribution. Near $L\approx 1$ Å the curve shows a sharp downward trend. Experimentally, L can be decreased by increasing the flux of ions and/or decreasing the transient-enhanced diffusion, perhaps by cooling.[18,23]

V. CONCLUSION

In conclusion, a model for the cluster size distributions arising during IBS is developed and studied using both kinetic Monte Carlo simulations and a self-consistent mean-field rate-equations theory. The two approaches give a quantitative description of the postimplantation experimental cluster size distributions. The self-consistent mean-field RE theory yields nearly quantitative agreement with KMC simulations. RE theory predicts that, under typical experimental conditions, the nanocluster size distribution asymptotes to a steady state. The steady-state shape of the nanocluster size distribution depends only on a characteristic length L whereas the average size cluster is influenced by the interface energy. The theory can be used to obtain information about the transient-enhanced diffusion coefficient and effective solubility during implantation, and to develop processing routes to narrow cluster size distributions.

ACKNOWLEDGMENTS

This work is supported by the Director, Office of Science, Office of Basic Energy Sciences, Materials Sciences and Engineering Division, of the U.S. Department of Energy under Contract No. DE-AC02-05CH11231.

[1] Y. M. Niquet, G. Allan, C. Delerue, and M. Lannoo, Appl. Phys. Lett. **77**, 1182 (2000).
[2] Y. Wang and H. Herron, J. Phys. Chem. **95**, 525 (1991).
[3] J. Zheng, C. Zhang, and R. M. Dickson, Phys. Rev. Lett. **93**, 077402 (2004).
[4] J. D. Blauwe, IEEE Trans. Nanotechnol. **77**, 1182 (2002).
[5] X. Peng, L. Manna, W. D. Yang, J. Wicham, E. Scher, A. Kadavanich, and A. P. Alivisatos, Nature (London) **404**, 59 (2000).
[6] V. Ramaswamy, T. E. Haynes, C. W. White, W. J. MoberlyChan, S. Roorda, and M. J. Aziz, Nano Lett. **5**, 373 (2005).
[7] J. G. Zhu, C. W. White, J. D. Budai, S. P. Withrow, and Y. Chen, J. Appl. Phys. **78**, 4386 (1995).
[8] J. D. Budai, C. W. White, S. P. Withrow, M. F. Chisholm, J. Zhu, and R. A. Zuhr, Nature (London) **390**, 384 (1997).
[9] K. H. Heinig, T. Müller, B. Schmidt, M. Strobel, and W. Möller, Appl. Phys. A: Mater. Sci. Process. **77**, 17 (2003).
[10] Q. Xu, I. D. Sharp, C. W. Yuan, D. O. Yi, A. M. G. C. Y. Liao, A. M. Minor, J. W. Beeman, M. C. Ridgway, J. W. A. III, D. C. Chrzan, and E. E. Haller, Phys. Rev. Lett. **97**, 155701 (2006).
[11] I. D. Sharp, D. O. Yi, Q. Xu, C. Y. Liao, J. W. Beeman, Z. Liliental-Weber, K. M. Yu, D. Zhakarov, J. W. A. III, D. C. Chrzan, and E. E. Haller, Appl. Phys. Lett. **86**, 063107 (2005).
[12] E. Cattaruzza, F. Gonella, G. Mattei, P. Mazzoldi, D. Gatteschi, C. Sangregorio, M. Falconieri, G. Salvetti, and G. Battaglin, Appl. Phys. Lett. **73**, 1176 (1998).
[13] C. Z. Jiang and X. J. Fan, Surf. Coat. Technol. **131**, 330 (2000).
[14] G. De Marchi, G. Mattei, P. Mazzoldi, and C. Sada, J. Appl. Phys. **92**, 4249 (2002).
[15] R. Giulian, P. Kluth, L. L. Araujo, D. J. Llewellyn, and M. C. Ridgway, Appl. Phys. Lett. **91**, 093115 (2007).
[16] G. Dearnaley, Nature (London) **256**, 701 (1975).
[17] T. Shinada, S. Okamoto, T. Kobayashi, and I. Ohdomari, Nature (London) **437**, 1128 (2005).
[18] N. E. B. Cowern and C. S. Rafferty, MRS Bull. **25**, 39 (2000).
[19] P. A. Stolk, H.-J. Gossmann, D. J. Eaglesham, D. C. Jacobson, C. S. Rafferty, G. H. Gilmer, M. Jaraiz, J. M. Poate, H. S. Luftman, and T. E. Haynes, J. Appl. Phys. **81**, 6031 (1997).
[20] D. O. Yi, M. H. Jhon, I. D. Sharp, Q. Xu, C. W. Yuan, C. Y. Liao, J. W. Ager III, E. E. Haller, and D. C. Chrzan, Phys. Rev. B **78**, 245415 (2008).
[21] I. D. Sharp, Q. Xu, C. Y. Liao, D. O. Yi, J. W. Beeman, Z. Liliental-Weber, K. M. Yu, D. Zhakarov, J. W. A. III, D. C. Chrzan, and E. E. Haller, J. Appl. Phys. **97**, 124316 (2005).
[22] C. W. Yuan, D. O. Yi, I. D. Sharp, S. J. Shin, C. Y. Liao, J. Guzman, J. W. Ager III, E. E. Haller, and D. C. Chrzan, Phys. Rev. Lett. **102**, 146101 (2009).
[23] L. Pelaz, G. H. Gilmer, V. C. Venezia, H.-J. Gossman, M. Jaraiz, and J. Barbolla, Appl. Phys. Lett. **74**, 2017 (1999).
[24] J. D. McBrayer, R. M. Swanson, and T. W. Sigmon, J. Electrochem. Soc. **133**, 1242 (1986).
[25] D. O. Yi, Ph.D. thesis, University of California, 2005.
[26] J. F. Ziegler, J. P. Biersack, and U. Littmark, *The Stopping and Range of Ions in Solids* (Pergamon, New York, 1985).
[27] R. Kissel and H. M. Urbassek, Nucl. Instrum. Methods Phys. Res. B **180**, 293 (2001).
[28] B. Satpati, J. Ghatak, P. V. Satyam, and B. N. Dev, J. Appl. Phys. **98**, 064904 (2005).
[29] G. S. Bales and D. C. Chrzan, Phys. Rev. B **50**, 6057 (1994).
[30] G. S. Bales and A. Zangwill, Phys. Rev. B **55**, R1973 (1997).
[31] C. M. Carbonaro, V. Fiorentini, and F. Bernardini, Phys. Rev. B **66**, 233201 (2002).
[32] G. I. Barenblatt, *Scaling*, 1st ed. (Cambridge University Press, Cambridge, England, 2003).
[33] J. G. Amar and F. Family, Phys. Rev. Lett. **74**, 2066 (1995).
[34] Due to the small number of points describing this distribution, the uncertainty in the value of L for Ag is substantial.